

An Integral View of Fast Shocks around Supernova 1006

Sladjana Nikolić^a, Glenn van de Ven^a, Kevin Heng^b, Daniel Kupko^c, Bernd Husemann^c, John C. Raymond^d, John P. Hughes^e,
Jesús Falcón-Barroso^f

^aMax Planck Institute for Astronomy, Königstuhl 17, D-69117, Heidelberg, Germany

^bUniversity of Bern, Center for Space and Habitability, Sidlerstrasse 5, CH-3012, Bern, Switzerland

^cLeibniz Institute for Astrophysics Potsdam (AIP), An der Sternwarte 16, D-14482 Potsdam, Germany

^dHarvard-Smithsonian Center for Astrophysics, 60 Garden Street, Cambridge, MA 02138, U.S.A.

^eDepartment of Physics and Astronomy, Rutgers University, 136 Frelinghuysen Road, Piscataway, NJ 08854, U.S.A.

^fInstituto de Astrofísica de Canarias, Vía Láctea, E38205, La Laguna (Tenerife), Spain

Supernova remnants are among the most spectacular examples of astrophysical pistons in our cosmic neighborhood. The gas expelled by the supernova explosion is launched with velocities $\sim 1000 \text{ km s}^{-1}$ into the ambient, tenuous interstellar medium, producing shocks that excite hydrogen lines. We have used an optical integral-field spectrograph to obtain high-resolution spatial-spectral maps that allow us to study in detail the shocks in the northwestern rim of supernova 1006. The two-component $H\alpha$ line is detected at 133 sky locations. Variations in the broad line widths and the broad-to-narrow line intensity ratios across tens of atomic mean free paths suggest the presence of suprathermal protons, the potential seed particles for generating high-energy cosmic-rays.

Supernova remnants, the expanding shells of material created in a stellar explosion, are astrophysical laboratories for studying non-thermal physics and high-velocity shocks, and have been scrutinized over a broad range of wavelengths. The signatures of non-thermal electrons are typically manifested in the X-ray, γ -ray and radio range of wavelengths [1]. Complementary to these observations, hydrogen emission from “Balmer-dominated shocks” [2, 3, 4], around supernova remnants of thermonuclear origin, directly probe the proton populations [5]. Until now, all studies of Balmer-dominated shocks have typically used conventional spectrographs that yield rich spectral information but limited spatial information. Here we report on Balmer-dominated shocks around a supernova remnant using integral-field unit (IFU) spectroscopy, a technique that produces a three-dimensional “data cube”: two dimensions of space (across the sky) and a spectral dimension. We selected supernova (SN) 1006 as our target, because it has a long history of serving as a laboratory for studying non-thermal physics and high-velocity shocks [6, 7, 8, 9, 10, 11, 12].

Long-slit spectroscopy, utilized in previous studies of Balmer-dominated shocks [13], cumulatively measures the $H\alpha$ emission emanating from regions much larger than the characteristic length scale: the mean free path for interactions between

hydrogen atoms and electrons or ions, $L_{\text{mfp}} \sim 1/n\sigma_{\text{ce}}$ (with n being the pre-shock number density and $\sigma_{\text{ce}} \sim 10^{-15} \text{ cm}^2$ denoting the typical cross section for charge exchange). Using the inferred range of densities for the northwestern rim of SN 1006 of n from 0.15 to 0.40 cm^{-3} [14, 15, 16], we estimated that the $0.''67$ size of a pixel in our IFU observations corresponds to $\sim 5L_{\text{mfp}}$. The high spatial resolution allowed us to separate out the contributions of bulk motion versus thermal velocity to the measured line widths, an issue which has limited the interpretation of previous observations. It also enabled us to study the spatial variation of the line widths and ratios and hence changes in microphysics of a shock across several atomic mean free paths. To buttress the second point, we have intentionally chosen a field of view that zooms in on a region of simple geometry, implying that any substantial spatial variation detected cannot be due to variations in density caused by geometric or projection effects.

Figure 1 illustrates the general configuration of our observations performed with VIMOS (VIisible Multi-Object Spectrograph) in the IFU mode on the VLT. We have focused on the northwestern rim, because it produces the brightest emission from a Balmer-dominated shock. As a first analysis of our data, we divided the shock structure into four strips and bin up the data along each strip. The two-component $H\alpha$ line is convincingly detected. To first order, the broad line width (FWHM) W yields the shock velocity v_s , whereas the level of energy equilibration between electrons and protons in the post-shock gas introduces small corrections [17, 18]. Because the broad line profile is a direct probe of the velocity distribution of the post-shock protons, and the narrow line profile traces pre-shock hydrogen atoms, the ratio of broad to narrow line intensities I_b/I_n contains information on how energy is shared between the pre- and post-shock regions. If no energy is shared, models which include the basic shock and atomic physics correctly translate the measured W and I_b/I_n values into the inferred v_s and β values [13, 19, 20, 21], where β is the ratio of electron to proton temperatures in the post-shock gas. Unusually low I_b/I_n values ($\lesssim 0.7$) indicate that suprathermal particles from the post-shock region are traveling upstream into the pre-shock gas and depositing energy via atomic interactions (excita-

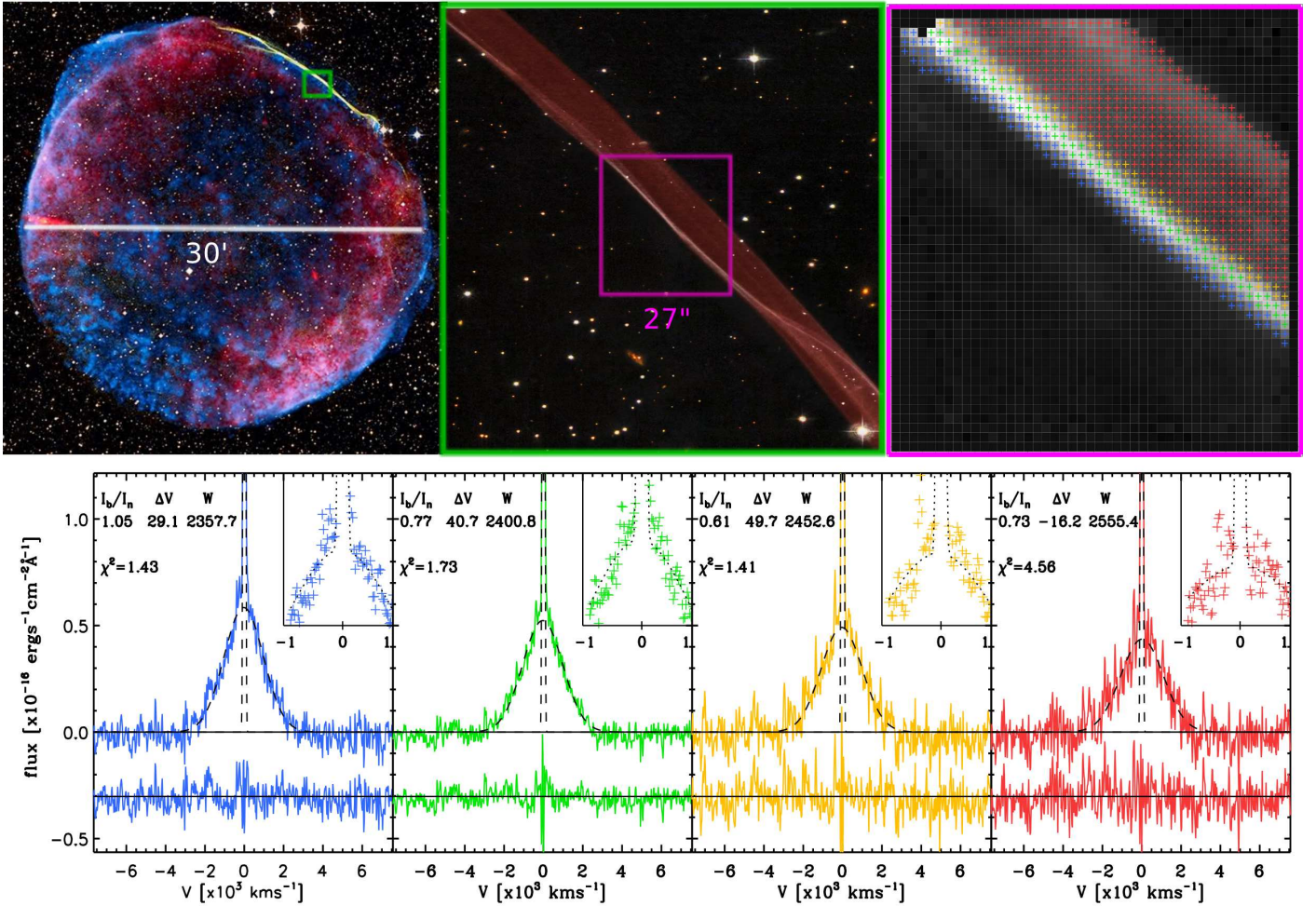


Figure 1: VIMOS-IFU spectroscopy of the shock front in the remnant of SN 1006. The *top-left* panel shows a composite image of the full remnant ($\approx 30'$ in diameter), combining data from the Very Large Array and Green Bank Telescope (red; NRAO/AUI/NSF/GBT/VLA/Dyer, Maddalena & Cornwell), Chandra X-ray Observatory (blue; NASA/CXC/Rutgers/G. Cassam-Chenaï, J. Hughes et al.), 0.9 m Curtis Schmidt optical telescope (yellow; NOAO/AURA/NSF/CTIO/Middlebury College/F. Winkler), and Digitized Sky Survey (orange and light blue stars). The green box indicates the region covered by the Hubble Space Telescope (HST) $H\alpha$ narrow-band image shown in the *top-middle*, with subsequently the magenta box indicating the region observed with the VIMOS-IFU. The *top-right* panel shows the reduced data cube collapsed in wavelength around the $H\alpha$ -line, recovering the shock front. The crosses with four different colors indicate the pixels for which the spectra have been combined to produce the spectra shown in the four panels at the *bottom*. In each of the bottom panels, the dashed black lines show the best-fit double-Gaussian, with parameters given in the legend: the intensity ratio of the broad to narrow component I_b/I_n , the velocity offset between the broad and narrow line centroids ΔV (in km s^{-1}), and width of the broad component W (in km s^{-1}). The reduced χ^2 values above unity along with the differences between the observed spectra and their best-fits (shown below the spectra with an offset of -0.3 for clarity), indicate that non-Gaussianity is present. Most of the reduced χ^2 values above unity come from the mismatching near the line core, as can be seen from the zoomed-in region ($-1000, 1000$) km s^{-1} in the top-right corner of bottom panels. On the horizontal axis is shown only the fitted region of the spectra, while the y axis shows the flux in units of $10^{-16} \text{ erg s}^{-1} \text{ cm}^{-2} \text{ \AA}^{-1}$ rescaled with the respect to the blue panel by factors 2 and 0.5 for the yellow and red panel, respectively.

tion, ionization and charge exchange), thus acting as precursors [22, 23, 24]. The loss of energy decreases the shock velocity and hence W . The increased flux of particles into the pre-shock region leads to enhanced excitation of the hydrogen atoms via collisions and increases I_n . The binned regions in Figure 1 already hint at this phenomenon, because $I_b/I_n \approx 0.6$ – 0.7 in two of the strips (yellow and red). The broad line exhibits subtle deviations from a Maxwellian profile in the line core, further supporting the presence of suprathermal particles in the shock.

We refined our approach by using the technique of Voronoi binning [25]. We combined neighbouring spectra into spatial Voronoi bins until S/N of about 40 was reached (see lower-right panel of Figure 2). We fitted double-Gaussians to the detected $H\alpha$ lines as shown in Section 2 of the Supplementary Materials (hereafter SM) and derived W and I_b/I_n values, thus producing the maps in the top-left and top-middle panel of Figure 2. In

addition to the lack of complex density variations, we demonstrated that the viewing geometry of the shock is simple: by measuring the velocity shift ΔV between the centroids of the narrow and broad $H\alpha$ line components, we derived the viewing angle θ via the relation $\Delta V = 3v_s \cos \theta / 4$. Our measurements indicate that $\theta \approx 80^\circ$ – 90° . Therefore, the shocks we observe are mostly edge-on as expected, but the rim seems slightly S-shaped along the line of sight as suggested by [14].

Surprisingly, we detected significant spatial variations in W and I_b/I_n across length scales $10''$ – $70L_{\text{mfp}}$, despite the simple geometry of the shocks, suggesting that they arise from variations in the microphysics rather than density. Within the bright rim the variations in W are of order 10–20%, significantly larger than the individual measurement uncertainties (see Section 2 and Table S1 in SM). The density variations of 20–40% required to explain the detected variations in W are much larger than

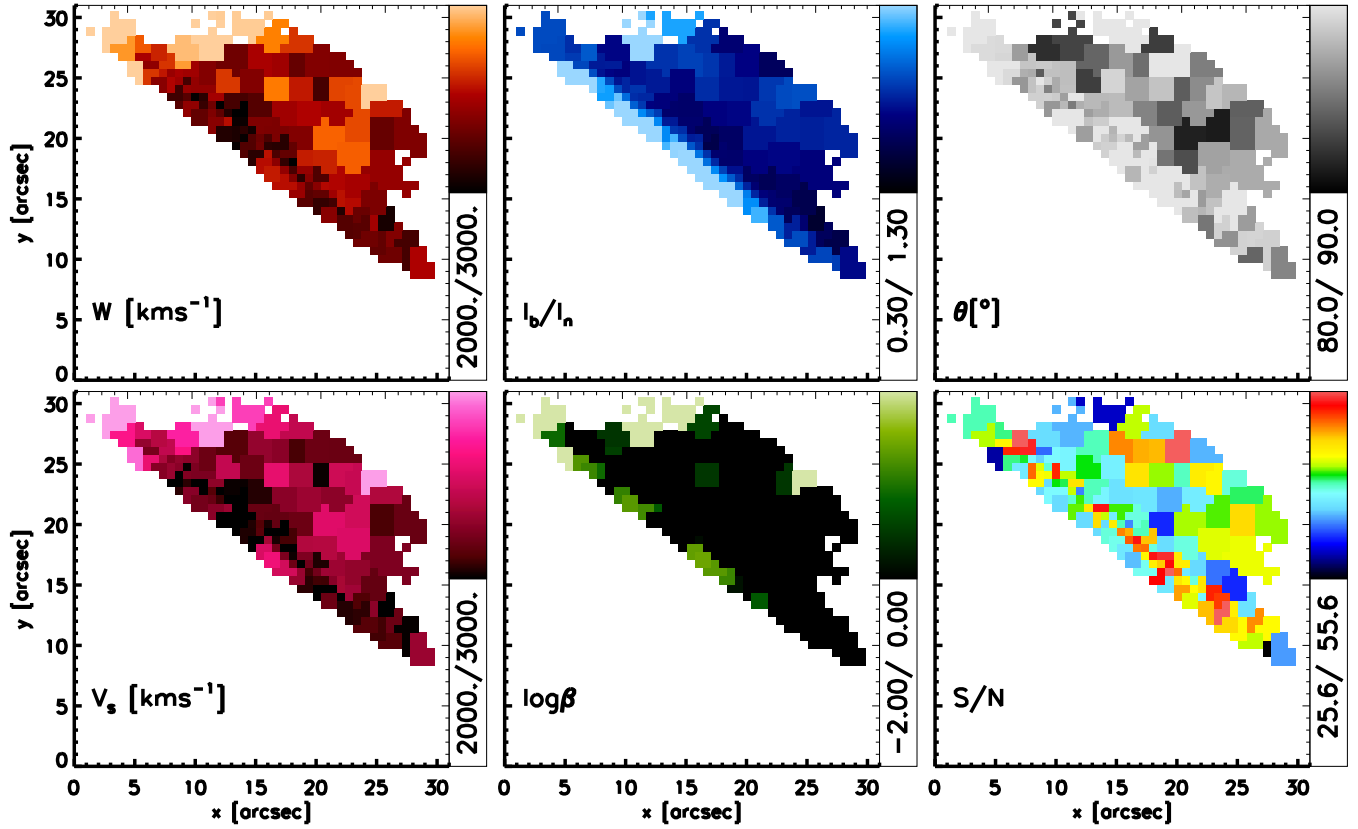


Figure 2: Two-dimensional spatial-spectral maps of various properties associated with the shock front in the remnant of SN1006. The *bottom-right* panel shows the spatial Voronoi binning to reach a minimum signal-to-noise $S/N \approx 40$. The maps in the *top row* from left to the right: the broad line width W (in km s^{-1}), the broad-to-narrow line intensity ratio I_b/I_n , and the shock inclination angle θ (in degrees). Shock velocities v_s and electron-to-proton temperature ratios β shown in the *bottom-left* and *bottom-middle* panels, respectively.

expected on these scales, and also incompatible with the unchanged smoothness of the shock over two decades of imaging observations [9, 14].

The low I_b/I_n values are found at all distances from the inner rim, reaching as low as 0.4 at some locations (Figure 3). We used the models without non-thermal physics to infer the values of v_s and β [19]. Most (about 85%) of the binned data are not accounted for by the model because of the low I_b/I_n values, thus motivating the need for models which include suprathermal particles and cosmic rays [26]. Combining the derived shock velocities with the proper motion measurement from [9], we obtained estimates of the heliocentric distance to SN 1006. Clearly, there has to be a unique distance, likely given by the upper points around ~ 2 kpc (see also Section 3 in SM). Most points, however, are underestimating the distance due to loss of energy from the broad line component resulting in too low inferred shock velocities.

These low values and variations of W and I_b/I_n , as well as the potential non-Gaussian contributions to the broad $\text{H}\alpha$ lines, demand an explanation. We examined three possibilities. The first is that “broad neutrals” are acting as a precursor [27, 28]. These are secondary populations of “hot” hydrogen atoms which are produced when post-shock protons capture an electron from a pre-shock hydrogen atom—the subsequent excitation of these broad neutrals produces the broad $\text{H}\alpha$ line component detected in our observations [2, 3, 4, 20]. Broad neutrals will warm the pre-shock gas and produce a third $\text{H}\alpha$ line component of

intermediate width, which may account for the narrow-plus-broad-line double-Gaussian being unable to fit the data within the measured uncertainties (i.e., not reaching a reduced χ^2 of unity). The strongest argument against broad neutrals is that they can only act as a precursor over an atomic mean free path, which is at odds with our observational result that the variations and low values of W and I_b/I_n extend over distances $\gg L_{\text{mfp}}$.

The second possibility is that pre-shock hydrogen atoms may cross the shock front, eventually become ionized and become protons gyrating along an ambient magnetic field line. It has been shown that these “pick-up protons” settle into a bi-spherical distribution which introduces a non-Gaussian contribution to the broad $\text{H}\alpha$ line core [29]. This explanation requires the magnetic field to be ordered on small length scales ($\ll L_{\text{mfp}}$), whereas turbulent magnetic fields will result in a broad $\text{H}\alpha$ line that is approximately Gaussian.

Both explanations are disfavored at low pre-shock neutral fractions, which is the situation in SN 1006 with a pre-shock neutral fraction of about 0.1 [13]. This is because both broad neutrals and pick-up ions require the pre-shock gas to contain a substantial population of hydrogen atoms (relative to electrons and protons) in order to initiate the process. In the limit of a fully ionized pre-shock gas, no broad neutrals or pick-up ions may be produced.

The explanation we favor is that the post-shock proton population includes a non-thermal sub-population of protons—suprathermal protons (that are not pick-up protons). Such an

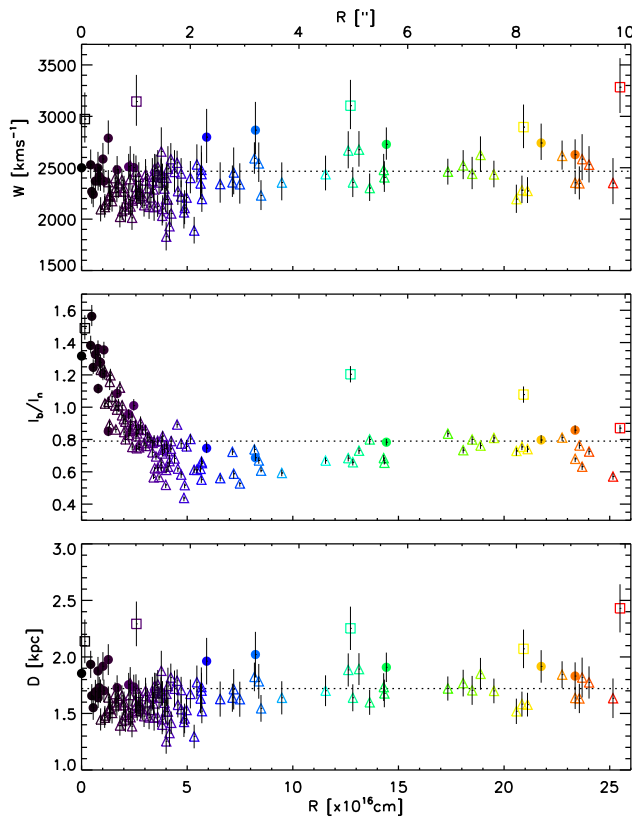


Figure 3: The three panels show all measured (with error bars) broad line widths W , broad-to-narrow intensity ratios I_b/I_n , and heliocentric distances D from combining the proper motion measurement with the shock velocities. Data are ordered in increasing distance from the inner rim (black/purple) to the outer rim (orange/red color), shown in arcsec at the top and in units of 10^{16} cm at the bottom horizontal axis. The inner rim coincides with the inner edge of the blue rim in the top-right panel in Figure 1. The dashed horizontal lines indicate the measured $W=2465.76$ km s $^{-1}$ and $I_b/I_n=0.79$ values from collapsing all spectra of the pixels on the shock front, and from there the inferred $D=1.72$ kpc. Data points marked with a filled circle are those for which a valid model solution is found. The triangles (squares) indicate that due to low (high) I_b/I_n values the models hit the lower (upper) boundary limit in β of 0.01 (1.0).

explanation requires no assumption on the magnetic field geometry or pre-shock neutral fraction. The lack of non-thermal X-ray and TeV γ -ray emission in the northwestern rim of the remnant indicates that if there is a CR precursor, the injection of electrons is little and the particle energies are low (< 1 MeV), but CR acceleration can still happen.

Our pilot project demonstrates the feasibility of using integral-field spectroscopy to observe and study the microphysics of high-velocity shocks around supernova remnants. The resulting high spatial resolution mapping of the Balmer dominated shocks in the northwestern rim of SN 1006 suggests the presence of suprathermal protons of energies 10-100 keV which can seed high-energy cosmic rays.

References

- [1] Reynolds, S.P. 2008, ARA&A, 46, 89
- [2] Chevalier, R.A., & Raymond, J.C. 1978, ApJ, 225, L27
- [3] Bychkov, K.V., & Lebedev, V.S. 1979, A&A, 80, 167
- [4] Chevalier, R.A., Kirshner, R.P., & Raymond, J.C. 1980, ApJ, 235, 186
- [5] Heng, K. 2010, PASA, 27, 23
- [6] Acero, F., et al. 2010, A&A, 516, A62
- [7] Koyama, K., et al. 1995, Nature, 378, 255
- [8] Berezhko, E.G., Ksenofontov, L.T. & Völk, H.J. 2002, A&A, 395, 943
- [9] Winkler, P. F., Gupta, G., & Long, K.S. 2003, ApJ, 585, 324

- [10] Rothenflug, R., Ballet, J., Dubner, G., Giacani, E., Decourchelle, A., & Ferrando, P. 2004, A&A, 425, 121
- [11] Cassam-Chenaï, G., Hughes, J.P., Reynoso, E.M., Badenes, C., & Moffett, D. 2008, ApJ, 680, 1180
- [12] Petruk, O., et al. 2009, MNRAS, 393, 1034
- [13] Ghavamian, P., Winkler, P.F., Raymond, J.C., & Long, K.S. 2002, ApJ, 572, 888
- [14] Raymond, J.C., Korreck, K.E., Sedlacek, Q.C., Blair, W.P., Ghavamian, P., & Sankrit, R. 2007, ApJ, 659, 1257
- [15] Long, K.S., Reynolds, S.P., Raymond J.C., Winkler, P.F., Dyer, K.K. & Petre, R. 2003, ApJ, 586, 1162
- [16] Acero, F., Ballet, J., & Decourchelle, A. 2007, A&A, 475, 883
- [17] Cargill, P.J., & Papadopoulos, K. 1988, ApJ, 329, L29
- [18] Ghavamian, P., Laming, J.M., & Rakowski, C.E. 2007, ApJ, 654, L69
- [19] van Adelsberg, M., Heng, K., McCray, R., & Raymond, J.C. 2008, ApJ, 689, 1089
- [20] Heng, K., & McCray, R. 2007, ApJ, 654, 923
- [21] Heng, K., van Adelsberg, M., McCray, R., & Raymond, J.C. 2007, ApJ, 668, 275
- [22] Ghavamian, P., Raymond, J., Hartigan, P., & Blair, W.P. 2000, ApJ, 535, 266
- [23] Sollerman, J., Ghavamian, P., Lundqvist, P., & Smith, R.C. 2003, A&A, 407, 249
- [24] Lee, J.-J., Koo, B.-C., Raymond, J., Ghavamian, P., Pyo, T.-S., Tajitsu, A., & Hayashi, M. 2007, ApJ, 659, L133
- [25] Cappellari, M., & Copin, Y. 2003, MNRAS, 342, 345
- [26] Morlino, G., Blasi, P., Bandiera, R., Amato, E., & Caprioli, D., arXiv:1211.6148
- [27] Lim, A.J., & Raga, A.C. 1996, MNRAS, 280, 103
- [28] Morlino, G., Bandiera, R., Blasi, P., & Amato, E. 2012, ApJ, 760, 137
- [29] Raymond, J.C., Isenberg, P.A., & Laming, J.M. 2008, ApJ, 682, 408

Acknowledgements: This work was supported by the IMPRS for Astronomy & Cosmic Physics at the University of Heidelberg. The paper is based on observations made with European Southern Observatory Telescopes at the La Silla Paranal Observatory under programme ID 085.D-0983.

Supplementary Materials

This Supplemental Material consists of three parts. The first part describes our integral-field spectroscopic observations and data reduction. This is followed by an assessment of the accuracy in fitting the $H\alpha$ emission line profile to extract the shock properties. Finally, we discuss estimates of the heliocentric distance to SN 1006. Figures S1 through S3 support the $H\alpha$ -profile fitting, with resulting parameters and uncertainties as well as shock properties given in Table S1.

1. Integral-field Spectroscopic Observations and Data Reduction

Our observations of the northwestern rim of SN 1006, were performed in queue mode on the nights of 2010 April 6, 11, 12, 13, and May 10, using the VIMOS (VIble Multi-Object Spectrograph) in the IFU (integral field unit) mode on the VLT. The IFU was placed approximately $15'$ away from the remnant's center, at coordinates $\alpha_{J2000} = 15^h02^m13^s.5$, $\delta_{J2000} = -41^\circ45'22''$. The overall exposure time of 6 hours accumulated in 10 exposures, all taken at air mass $\lesssim 1.60$ and seeing $\lesssim 1''.60$, enabled us to collect enough photons to reach the required signal-to-noise ratios (S/N). A dither pattern with small offsets between the individual exposures was applied in order to account for dead fibers. We have used a spatial scale of $0''.67$ per pixel in combination with the HR-Orange grism providing a field-of-view of $27'' \times 27''$ as well as a resolution of $R \approx 2650$ within the wavelength range of $5250 \text{ \AA} \lesssim \lambda \lesssim 7400 \text{ \AA}$.

The data has been reduced with our own dedicated data reduction pipeline which was developed in particular to deal with the rather complex VIMOS instrument in IFU mode. It is based on several individual scripts written in the software language python. VIMOS is made of four identical optical quadrants, each representing a completely independent spectrograph. Each quadrant is at first reduced separately, including the following standard procedures: bias subtraction, stray-light correction, interactive fibre-identification and -tracing, spectra extraction and wavelength calibration using the arclamp frames. For the extraction of the fluxes the “optimal extraction algorithm” was applied [30], which was designed to deal with dense packed IFUs to correct for the cross talk between adjacent fibres. The associated continuum lamp frames were used to construct corresponding fibre-flatfields which were used to normalise the wavelength-dependent throughput of each fibre. Additionally, VIMOS also suffers from substantial distortions on the raw frames due to instrumental flexure. Thus, in order to guarantee the best possible extraction results the fiber traces were smoothed and corrected for shifts between science and calibration frames. This included a 2nd order correction of the absolute positions of the traces as well as an adjustment of the wavelength solution by using the available strong night-sky emission lines within the observed wavelength-range. The raw frames were cleaned for cosmic rays using the newly developed software package PyCosmics [31], which represents an optimized algorithm to detect their artifacts in IFU raw-data.

After the basic reduction steps the four individual science frames for each observing block were combined and rearranged into three dimensional datacubes, using the dedicated VIMOS lookup-tables. Flux calibration was achieved by reduction and extraction of photometric standard stars which were observed using the same setup as the science data. As the VIMOS-IFU does not have “sky-dedicated” fibers, it is normal practice to do separate offset “sky exposures”, but in this case the sky background could be reliably measured from the “empty” downward triangular part in the field-of-view (see top-right panel of Fig-

ure 1). The last step involved the correction of the barycentric Doppler shift, i.e., the offset in velocity space caused by the movement of the Earth around the Sun. The observations were accomplished within a time-window of approximately one month, causing a velocity shift of about 20 km s^{-1} which corresponds roughly to one pixel on the detector. In order to readjust this offset we measured the center of the narrow $H\alpha$ emission line and shifted it to the laboratory wavelength of 6562.8 \AA .

The $H\alpha$ line is found in the middle of the HR-Orange grism wavelength range of $5250\text{--}7400 \text{ \AA}$. This spectral range is broad enough to both easily fit the broad component of the $H\alpha$ line with width of the order of 50 \AA , and to still leave plenty of spectral range for an accurate determination of the continuum. Finally, we used the precise header information of the telescope-pointings to compute the spatial-offsets between each observation and combined all ten individual datacubes within one final cube, containing in total 2162 spectra. The instrumental resolution of about 110 km s^{-1} (FWHM) around the wavelength of $H\alpha$ is more than sufficient to measure the width of the broad line of $2000\text{--}3000 \text{ km s}^{-1}$, as well as deviations from a Gaussian profile. The width of the narrow line, expected to be about 20 km s^{-1} , cannot be resolved, but the narrow line intensity can be accurately measured, especially given that the narrow line has a significantly higher S/N than the broad line.

2. Accuracy of the $H\alpha$ -line fitting

We fitted the $H\alpha$ -line with two Gaussians, one for the narrow component and the other for the broad component, after convolving with a Gaussian instrumental profile. Hint on the non-Gaussianity around the line core of the broad component that we detected is a supporting, but not the main piece of evidence of suprathermal protons presence.

In order to investigate possible non-physical contributions to the $H\alpha$ -line profile, we compared the continuum emission profile across wavelength in the region downstream and upstream of the shock. As shown in Figure S1, we combined spectra in the downstream and upstream regions. The continuum has the same profile in these two regions, and does not affect the $H\alpha$ -line profile. In these regions we did, however, detect diffuse narrow-line $H\alpha$ emission, with surface brightness, 10-30 times lower compared to the emission in the four regions in Figure 1.

Next, to verify that the instrumental profile is Gaussian we fitted sky lines that went through the same data reduction steps (except for sky subtraction). In Figure S2, we show five sky lines around $H\alpha$ line fitted with a Gaussian. The fits together with the differences between the observed and fitted sky lines show that the instrumental profile is indistinguishable from Gaussian.

We have also checked if the residuals might be coming from the intrinsic variations among the individual spectra that went into the combined spectra. The offsets between velocity centroids are much smaller than the “extra-core” size, and thus rule out this possibility. Also, the individual bins have very similar narrow line widths that are always unresolved, but much smaller than the “extra-core” size.

Finally, the uncertainties in measuring the broad line width W and broad-to-narrow intensity ratio I_b/I_n were determined in various independent ways, taking into account the varying noise per pixel in wavelength as given by the derived error spectrum per pixel. Two of the methods were very robust and led to consistent error estimates even in case of spectra with signal-to-noise significantly lower than our target $S/N \approx 40$. In the first method, we created 1000 mock spectra per Voronoi bin through Monte Carlo sampling of the observed (combined) spectrum, and fitted each mock spectrum with a double Gaussian. The resulting distributions of values in W and I_b/I_n shows that

both quantities are uncorrelated and their means are the same as from the fit to the observed spectrum. Their standard deviations, however, are slightly larger than those from the second method in which we varied¹ W and I_b/I_n on a grid around their best-fit values until χ^2 changed by an amount corresponding to the 68% confidence level given the degrees of freedom. This is expected, as the first method, apart from the added noise from the error spectrum, also includes noise already inherent in the observed spectrum, increasing the reduced χ^2 values of the mock spectra fits above unity. Re-scaling the reduced χ^2 values to unity leads to uncertainties that are fully consistent with those inferred from the second method. The double-Gaussian fits to the $H\alpha$ -line profile in all 133 sky positions are shown in Figure S3. The resulting best fit parameters and uncertainties are given in Table S1, along with shock properties inferred using van Adelsberg models.

3. Heliocentric distance to SN 1006

When converting from angular to physical length scales, $1'' \approx 2.58 \times 10^{16}$ cm, we adopted a heliocentric distance of 1.72 kpc, derived as follows. We first summed up all pixels on the shock front, and extracted the width of the broad component W and intensity ratio I_b/I_n by fitting the $H\alpha$ line with double-Gaussians. The resulting broad line width and broad-to-narrow intensity ratio are $W = 2466 \text{ km s}^{-1}$ and $I_b/I_n = 0.79$. Using the van Adelsberg et al. model, this yields a shock velocity of $v_s = 2288 \text{ km s}^{-1}$. Combining this shock velocity with the proper motion measurements of 280 mas yr^{-1} [9] yields a heliocentric distance of 1.72 kpc.

Previously inferred distances to SN 1006 from the $H\alpha$ observations in the northwestern rim, 2.18 kpc [9] and 1.6 kpc [19], were based on long-slit spectroscopic observations from [13]. The discrepancy in the inferred distances comes from different shock models applied. The latter one uses the same van Adelsberg et al. model, yielding a lower shock velocity for the same $W = 2290 \text{ km s}^{-1}$ and $I_b/I_n = 0.84$, primarily due to the broad neutral velocities contribution to the relative speeds in fast neutral-ion interactions.

Analysis of the optical spectrum of the Schweizer-Middleditch star [32] which lies almost at the same line-of-sight as the center of SN 1006, sets the upper limit on the distance of SN 1006 at 2.1 kpc. The observed ejecta expansion at 7026 km s^{-1} [33], and the requirement that this material lie within the remnant places a lower limit of 1.6 kpc. We actually expect the distance to be closer to ~ 2 kpc to explain the upper envelope of the points in Figure 3, but a model that properly takes into account the non-thermal physics is needed before we can robustly measure an intrinsic shock velocity and correspondingly obtain a secure estimate of the heliocentric distance.

References

- [30] Sharp, R., & Birchall, M.N. 2010, PASA, 27, 91
- [31] Husemann, B., Kamann, S., Sandin, C., Sanchez, S.F., Garcia-Benito, R., & Mast, D. 2012, A&A, 545, A137
- [32] Burleigh, M. R., Heber, U., O'Donoghue, D., & Barstow, M. A. 2000, A&A, 356, 585
- [33] Hamilton, A. J. S., Fesen, R. A., & Blair, W. P. 2007, MNRAS, 381, 771

¹Keeping the total intensity $I_n + I_b$, narrow line width and centroids of the narrow and broad component fixed to their best-fit values.

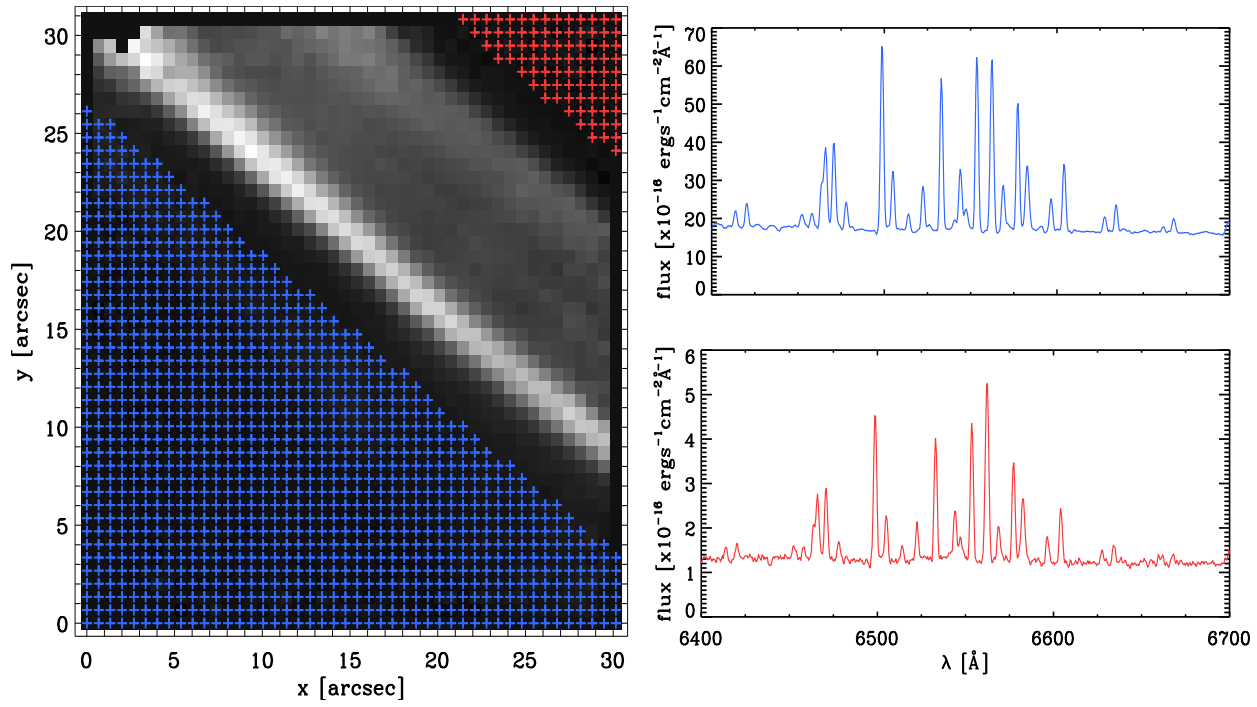


Figure S1: The *left* panel shows the reduced data cube collapsed in wavelength around the $H\alpha$ -line with blue and red crosses indicating the pixels for which the combined non-sky-subtracted spectra are shown in the *right* panels. Comparing the continuum emission across wavelength, we confirm that the emission profile is the same in the upstream and downstream region of the shock.

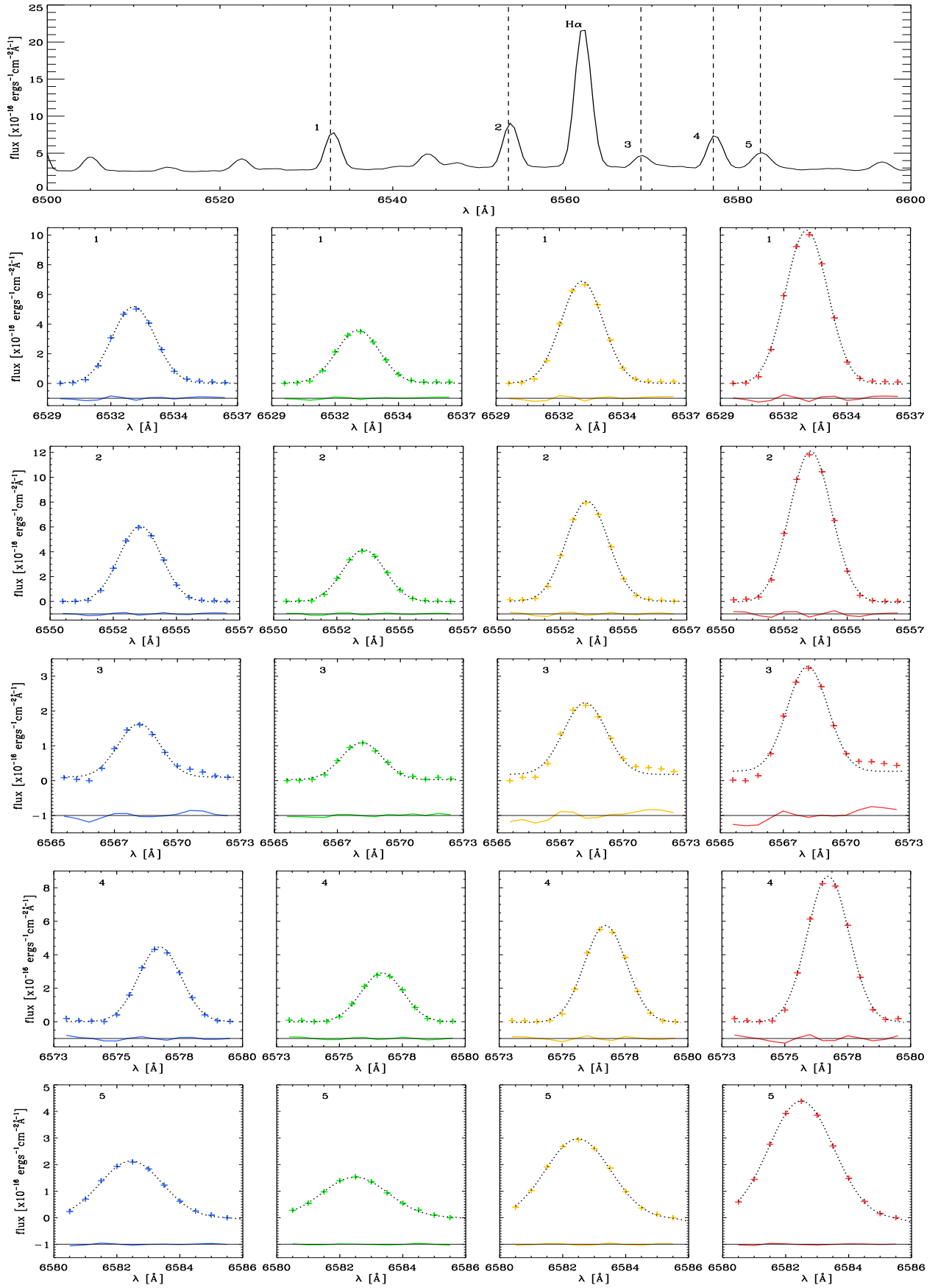


Figure S2: The *top* panel shows a non-sky-subtracted spectrum with five sky lines around H α , indicated by vertical dashed lines and numbered. Next, each *row* shows one sky line fitted with a Gaussian for the four different regions consistent with the ones in Figure 1. The fits along with the differences between observed and fitted sky lines (with an offset downward for clarity) show that the instrumental profile is Gaussian.

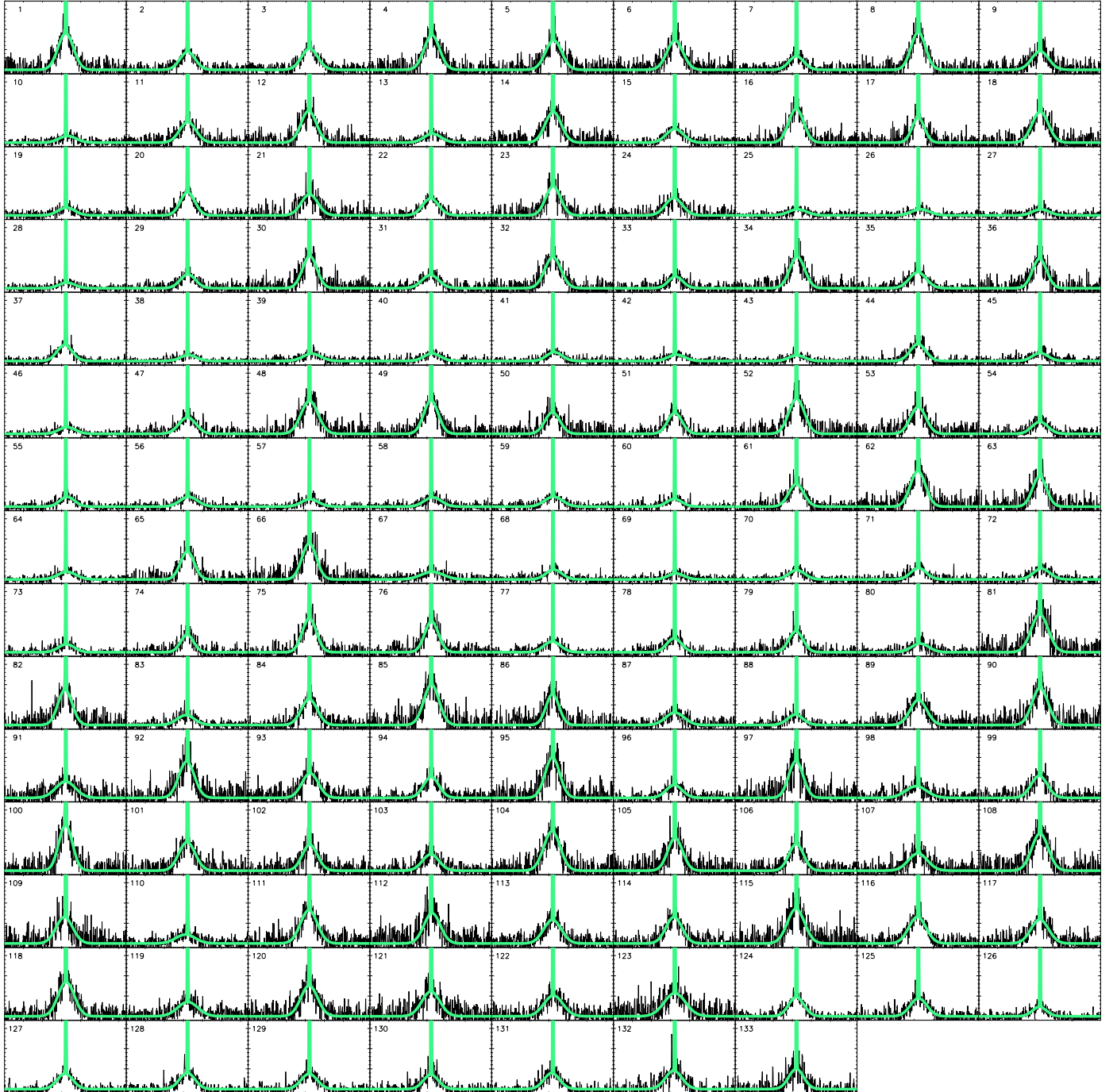


Figure S3: Montage of the $H\alpha$ line profiles in each of the 133 Voronoi bins. The horizontal axis represents wavelengths and vertical axis is in the relative units. Over-plotted are the double-Gaussian fits to the narrow and broad line components. No smoothing has been applied to the data.

Table S1: Properties of the shock front in the remnant of SN 1006 for 133 spatially binned locations. Columns 1–5: number of the (Voronoi) bin, x and y coordinates of the bin centroid, number of combined pixels, and signal-to-noise ratio. Columns 6–10: measured values of the broad component W and the broad-to-narrow line intensity ratio I_b/I_n (both with estimated uncertainties based on χ^2 68% confidence levels), shock inclination angle i (with typical uncertainty of 1.6° coming from a typical error of 47 km s^{-1} in ΔV), and the reduced χ^2 of the double-Gaussian fit to the observed H α -line. Columns 10–11: shock velocity v_s and electron-to-proton ratio β (in base-10 logarithm) of the best-fit shock model; a long dash indicates when the shock model hits the adopted boundary limits of $\log \beta = (-2, 0)$, likely because CR physics is missing.

Bin	x	y	Spx	S/N	W_{obs} km s $^{-1}$	$(I_b/I_n)_{\text{obs}}$	i_{obs} $^\circ$	red. χ^2	v_s km s $^{-1}$	$\log \beta$
(1)	(2)	(3)	(4)	(5)	(6)	(7)	(8)	(9)	(10)	(11)
1	19.43	16.08	1	52.68	2268 (+110/-94)	0.93 (+0.03/-0.03)	89.3	0.91	2088	—
2	19.43	15.38	3	36.57	2242 (+134/-126)	1.25 (+0.05/-0.04)	89.7	0.78	2058	-1.86
3	18.76	16.03	3	50.67	2417 (+110/-102)	1.28 (+0.03/-0.04)	89.1	0.91	2294	-0.95
4	20.10	15.41	1	44.70	2267 (+110/-102)	0.98 (+0.03/-0.03)	86.9	0.82	2087	—
5	20.10	16.08	1	48.21	2376 (+141/-134)	0.76 (+0.02/-0.03)	87.2	0.81	2194	—
6	19.43	16.75	1	50.81	2370 (+141/-126)	0.78 (+0.02/-0.03)	89.2	0.78	2189	—
7	20.24	16.79	3	44.35	2219 (+157/-141)	0.58 (+0.02/-0.02)	89.5	0.81	2041	—
8	18.76	16.75	1	45.85	2124 (+94/-94)	0.89 (+0.03/-0.03)	89.5	0.75	1948	—
9	20.77	16.08	1	36.70	2490 (+220/-188)	0.63 (+0.03/-0.03)	89.9	0.72	2313	—
10	20.93	18.06	8	38.61	2542 (+204/-181)	0.67 (+0.02/-0.02)	82.7	1.28	2368	—
11	18.85	17.42	2	51.71	2406 (+134/-126)	0.71 (+0.02/-0.02)	89.3	0.92	2226	—
12	20.77	15.41	1	43.55	2266 (+118/-110)	0.77 (+0.02/-0.03)	86.7	0.81	2086	—
13	18.90	18.18	4	36.01	2531 (+196/-173)	0.61 (+0.02/-0.02)	84.6	0.86	2357	—
14	18.09	16.75	1	44.23	2360 (+118/-110)	1.03 (+0.03/-0.04)	88.9	0.85	2179	—
15	17.76	16.39	4	38.21	2499 (+134/-118)	1.32 (+0.05/-0.04)	89.7	0.89	2461	-0.81
16	18.09	17.42	1	51.08	2199 (+102/-94)	0.84 (+0.03/-0.02)	88.1	0.83	2021	—
17	18.09	18.09	1	38.59	1829 (+141/-134)	0.61 (+0.02/-0.02)	89.5	0.97	1663	—
18	17.42	17.42	1	43.81	2399 (+126/-118)	1.01 (+0.04/-0.03)	89.5	0.79	2218	—
19	21.60	16.22	5	35.75	2479 (+236/-204)	0.55 (+0.02/-0.02)	87.4	0.93	2302	—
20	20.62	14.74	3	46.98	2143 (+102/-94)	1.02 (+0.02/-0.03)	89.8	0.79	1966	—
21	21.44	15.41	1	38.59	2432 (+165/-157)	0.66 (+0.03/-0.02)	89.6	0.89	2252	—
22	21.36	14.01	4	42.77	2372 (+110/-94)	1.12 (+0.03/-0.03)	87.6	0.87	2175	-1.31
23	21.44	14.74	1	43.37	2181 (+149/-126)	0.75 (+0.03/-0.02)	89.4	0.83	2003	—
24	22.11	14.82	2	44.82	2507 (+165/-149)	0.63 (+0.02/-0.02)	86.3	0.82	2331	—
25	22.76	18.73	14	42.71	2667 (+188/-173)	0.68 (+0.02/-0.02)	85.8	1.40	2502	—
26	21.09	20.26	12	41.81	2676 (+181/-165)	0.73 (+0.02/-0.02)	81.3	1.25	2512	—
27	23.05	15.86	8	33.32	2454 (+243/-212)	0.59 (+0.02/-0.03)	86.8	1.01	2275	—
28	18.79	20.23	8	31.57	2356 (+196/-173)	0.59 (+0.02/-0.02)	85.3	1.10	2175	—
29	17.54	18.78	3	46.08	2272 (+134/-134)	0.62 (+0.01/-0.02)	88.8	0.95	2091	—
30	17.42	18.09	1	48.11	2135 (+118/-110)	0.78 (+0.03/-0.02)	88.4	0.82	1959	—
31	16.72	17.39	4	35.13	2528 (+149/-134)	1.38 (+0.06/-0.05)	87.2	0.86	2567	-0.71
32	16.75	18.09	1	47.90	2379 (+110/-102)	0.95 (+0.03/-0.02)	89.4	0.80	2198	—
33	16.86	19.45	3	39.35	2108 (+173/-157)	0.52 (+0.01/-0.02)	86.1	1.06	1933	—
34	16.75	18.76	1	51.06	2211 (+110/-102)	0.79 (+0.02/-0.02)	87.2	0.84	2032	—
35	22.80	14.22	3	49.91	2493 (+141/-134)	0.62 (+0.01/-0.02)	87.6	0.87	2316	—
36	22.11	14.07	1	37.59	2095 (+141/-126)	0.80 (+0.03/-0.03)	87.2	0.79	1920	—
37	22.61	13.32	5	46.21	2228 (+102/-94)	0.89 (+0.02/-0.02)	84.5	0.98	2050	—
38	25.73	17.29	22	42.98	2406 (+157/-141)	0.66 (+0.02/-0.01)	86.5	1.49	2226	—

Bin	x "	y "	Spx	S/N	W_{obs} km s^{-1}	$(I_b/I_n)_{\text{obs}}$	i_{obs} °	red. χ^2	v_s km s^{-1}	$\log \beta$
(1)	(2)	(3)	(4)	(5)	(6)	(7)	(8)	(9)	(10)	(11)
39	23.52	21.21	11	41.18	2624 (+181/-165)	0.76 (+0.02/-0.02)	80.4	1.28	2456	—
40	21.88	22.28	9	36.97	2441 (+165/-149)	0.80 (+0.02/-0.03)	85.7	1.20	2262	—
41	25.39	20.75	12	45.41	2281 (+141/-126)	0.75 (+0.02/-0.02)	83.6	1.24	2101	—
42	19.31	22.20	9	34.71	2478 (+157/-141)	0.68 (+0.02/-0.02)	83.0	1.30	2300	—
43	24.61	14.80	9	31.54	2339 (+204/-188)	0.53 (+0.01/-0.02)	88.4	1.00	2158	—
44	23.49	13.67	3	49.25	2289 (+126/-118)	0.57 (+0.02/-0.01)	88.5	0.93	2109	—
45	16.63	20.46	5	38.63	2341 (+212/-181)	0.56 (+0.02/-0.02)	89.7	1.06	2160	—
46	17.48	22.25	8	36.44	2437 (+181/-157)	0.67 (+0.02/-0.02)	84.5	1.13	2258	—
47	16.03	18.09	3	36.60	2498 (+157/-141)	1.36 (+0.05/-0.05)	89.3	0.86	2490	-0.76
48	16.08	18.76	1	48.57	2509 (+126/-118)	0.96 (+0.03/-0.03)	89.5	0.80	2328	-1.90
49	16.08	19.43	1	46.59	2124 (+110/-102)	0.79 (+0.02/-0.03)	89.1	0.67	1949	—
50	16.08	20.10	1	33.76	2210 (+173/-165)	0.76 (+0.04/-0.03)	87.5	0.83	2031	—
51	15.36	18.75	3	38.40	2117 (+110/-102)	1.22 (+0.04/-0.05)	90.0	0.93	1941	—
52	15.41	19.43	1	47.63	2313 (+126/-118)	0.89 (+0.03/-0.02)	89.5	0.87	2133	—
53	15.41	20.10	1	39.34	2297 (+165/-149)	0.75 (+0.03/-0.03)	89.0	0.63	2117	—
54	15.19	21.11	4	41.04	2347 (+173/-149)	0.62 (+0.02/-0.02)	89.2	0.92	2166	—
55	20.45	24.40	6	39.26	2194 (+141/-134)	0.73 (+0.02/-0.03)	83.2	1.06	2016	—
56	21.87	24.37	7	44.35	2615 (+149/-134)	0.81 (+0.02/-0.02)	85.6	1.16	2446	—
57	18.87	24.37	9	41.68	2522 (+149/-134)	0.73 (+0.02/-0.02)	87.5	1.37	2348	—
58	25.24	22.42	8	39.97	2529 (+181/-173)	0.73 (+0.02/-0.02)	83.5	1.00	2355	—
59	23.15	23.69	7	43.80	2627 (+149/-141)	0.86 (+0.03/-0.02)	87.7	0.97	2430	-1.57
60	15.20	22.50	8	36.31	2230 (+149/-141)	0.61 (+0.02/-0.01)	88.0	1.25	2051	—
61	14.65	19.43	3	38.76	2220 (+110/-102)	1.20 (+0.04/-0.04)	88.6	0.91	2042	—
62	14.74	20.10	1	44.37	2225 (+118/-118)	0.86 (+0.03/-0.03)	88.0	0.75	2046	—
63	14.74	20.77	1	36.95	2055 (+126/-118)	0.79 (+0.03/-0.03)	87.0	0.78	1881	—
64	16.76	24.21	9	44.92	2727 (+165/-149)	0.78 (+0.02/-0.02)	86.1	1.20	2533	-1.57
65	14.07	20.10	2	35.87	2022 (+110/-102)	1.12 (+0.04/-0.05)	88.2	0.80	1849	—
66	14.07	20.77	1	42.29	2120 (+134/-118)	0.81 (+0.03/-0.03)	89.0	0.84	1944	—
67	24.64	23.59	7	38.71	3284 (+283/-251)	0.87 (+0.02/-0.03)	86.8	0.92	3225	—
68	27.50	20.46	16	41.68	2348 (+165/-157)	0.76 (+0.02/-0.02)	86.1	1.13	2168	—
69	21.78	25.62	9	34.81	2350 (+243/-204)	0.57 (+0.02/-0.02)	84.2	1.12	2169	—
70	20.09	26.04	11	53.82	2354 (+118/-110)	0.68 (+0.01/-0.02)	88.9	1.36	2173	—
71	18.43	26.20	6	46.42	2275 (+134/-118)	0.74 (+0.02/-0.02)	89.1	1.26	2094	—
72	17.12	26.42	6	46.57	2435 (+134/-126)	0.81 (+0.02/-0.03)	83.7	1.09	2256	—
73	14.81	24.92	9	37.19	2356 (+149/-141)	0.66 (+0.02/-0.02)	87.7	1.27	2175	—
74	13.66	22.13	3	37.38	1889 (+134/-126)	0.61 (+0.02/-0.02)	86.9	0.96	1720	—
75	13.40	20.66	2	45.33	2078 (+ 86/-86)	1.01 (+0.03/-0.03)	89.7	0.88	1903	—
76	13.59	21.44	2	51.06	2032 (+102/-94)	0.74 (+0.03/-0.02)	88.2	0.84	1859	—
77	15.49	26.61	9	47.53	2462 (+126/-126)	0.84 (+0.02/-0.02)	86.8	1.09	2284	—
78	12.91	22.88	5	39.35	2196 (+134/-126)	0.65 (+0.02/-0.02)	87.2	1.06	2018	—
79	12.67	20.72	4	35.90	2096 (+118/-118)	1.23 (+0.05/-0.04)	86.8	1.07	1921	—
80	18.31	27.56	8	35.97	2583 (+243/-204)	0.63 (+0.02/-0.02)	82.7	1.14	2412	—
81	12.73	21.44	1	44.55	2502 (+134/-126)	1.01 (+0.04/-0.03)	88.3	0.86	2301	-1.31
82	12.73	22.11	1	39.36	2099 (+134/-134)	0.82 (+0.03/-0.04)	86.3	0.78	1924	—
83	12.38	24.51	8	40.66	2591 (+157/-149)	0.74 (+0.03/-0.02)	82.6	1.13	2420	—
84	11.83	21.44	3	41.26	2369 (+118/-110)	1.35 (+0.05/-0.05)	89.1	0.82	2258	-0.91
85	12.06	22.11	1	41.05	2259 (+134/-126)	0.90 (+0.04/-0.04)	89.1	0.74	2080	—
86	12.06	22.78	1	33.65	1931 (+157/-141)	0.67 (+0.04/-0.03)	87.6	0.82	1761	—

Bin	x "	y "	Spx	S/N	W_{obs} km s^{-1}	$(I_b/I_n)_{\text{obs}}$	i_{obs} °	red. χ^2	v_s km s^{-1}	$\log \beta$
(1)	(2)	(3)	(4)	(5)	(6)	(7)	(8)	(9)	(10)	(11)
87	16.59	27.92	10	42.13	2741 (+188/-165)	0.80 (+0.03/-0.02)	89.4	0.95	2543	-1.45
88	13.41	26.38	11	39.36	2302 (+141/-126)	0.80 (+0.02/-0.03)	84.4	1.24	2122	—
89	11.54	23.45	2	44.96	2444 (+149/-134)	0.77 (+0.03/-0.03)	89.6	0.77	2265	—
90	11.39	22.11	1	38.93	2348 (+141/-141)	1.01 (+0.04/-0.04)	89.7	0.88	2167	—
91	14.48	29.13	12	29.53	2895 (+220/-204)	1.08 (+0.05/-0.05)	89.0	1.11	2749	—
92	11.39	22.78	1	42.26	2302 (+149/-141)	0.81 (+0.03/-0.03)	85.4	0.93	2122	—
93	10.94	24.12	2	42.12	2400 (+165/-149)	0.80 (+0.03/-0.03)	86.9	0.80	2220	—
94	10.62	22.08	4	35.85	2268 (+126/-118)	1.56 (+0.07/-0.06)	90.0	0.92	2199	-0.80
95	10.72	22.78	1	37.78	2151 (+134/-118)	0.91 (+0.04/-0.04)	87.2	0.76	1975	—
96	10.99	25.06	6	37.39	2357 (+165/-141)	0.72 (+0.02/-0.02)	87.6	1.15	2176	—
97	10.72	23.45	1	40.19	2117 (+149/-134)	0.79 (+0.04/-0.03)	86.8	0.81	1941	—
98	11.35	27.51	15	34.79	3103 (+251/-228)	1.20 (+0.05/-0.05)	82.9	1.19	2990	—
99	9.97	22.78	3	37.83	2392 (+126/-118)	1.28 (+0.05/-0.05)	86.1	0.91	2253	-0.98
100	10.05	23.45	1	40.63	2013 (+118/-118)	0.94 (+0.03/-0.04)	88.6	0.80	1840	—
101	10.05	24.25	2	49.73	2402 (+134/-126)	0.77 (+0.02/-0.03)	87.2	0.95	2222	—
102	9.38	23.45	2	35.76	2237 (+157/-149)	1.16 (+0.05/-0.05)	87.9	0.94	2058	—
103	9.50	25.48	3	37.77	2438 (+212/-188)	0.66 (+0.03/-0.02)	87.8	0.90	2259	—
104	9.38	24.12	1	43.11	2412 (+141/-126)	0.86 (+0.03/-0.03)	85.6	0.70	2232	—
105	9.38	24.79	1	38.80	2191 (+165/-141)	0.73 (+0.04/-0.03)	88.2	0.85	2013	—
106	8.70	24.02	3	43.51	2175 (+118/-102)	1.06 (+0.04/-0.04)	88.4	0.97	1998	—
107	8.81	26.13	2	33.06	2797 (+275/-251)	0.75 (+0.04/-0.03)	88.3	0.72	2605	-1.51
108	8.71	24.79	1	42.75	2435 (+149/-134)	0.86 (+0.03/-0.04)	89.4	0.82	2256	—
109	8.71	25.46	1	35.53	2459 (+212/-196)	0.68 (+0.03/-0.03)	83.7	0.80	2281	—
110	9.12	27.02	9	36.01	2866 (+275/-236)	0.69 (+0.03/-0.02)	82.4	1.03	2683	-1.59
111	8.04	24.64	2	48.25	2480 (+134/-126)	1.09 (+0.04/-0.03)	87.9	0.87	2294	-1.17
112	8.04	25.46	1	37.72	2413 (+181/-173)	0.72 (+0.03/-0.03)	86.1	0.89	2233	—
113	7.65	26.19	3	51.42	2583 (+157/-141)	0.74 (+0.02/-0.02)	87.9	0.79	2412	—
114	7.26	24.74	3	36.79	2370 (+134/-118)	1.33 (+0.05/-0.05)	86.4	0.83	2245	-0.94
115	7.37	25.46	1	40.42	2521 (+188/-165)	0.87 (+0.04/-0.03)	87.5	0.77	2346	—
116	6.86	26.94	4	55.60	2548 (+118/-110)	0.89 (+0.02/-0.02)	86.1	0.86	2375	—
117	6.55	25.46	3	39.74	2585 (+157/-141)	1.21 (+0.05/-0.04)	88.5	0.84	2545	-0.83
118	6.49	26.13	2	49.78	2388 (+126/-110)	0.85 (+0.03/-0.03)	88.7	0.75	2208	—
119	5.25	26.03	5	28.79	2973 (+259/-228)	1.49 (+0.08/-0.07)	89.6	0.86	2837	—
120	5.79	26.80	2	43.83	2462 (+157/-149)	0.82 (+0.03/-0.03)	89.1	0.83	2284	—
121	5.64	27.51	3	39.74	2658 (+236/-212)	0.79 (+0.03/-0.04)	88.6	0.83	2492	—
122	4.32	27.29	6	41.85	2788 (+173/-157)	0.85 (+0.03/-0.03)	88.7	0.77	2623	-1.18
123	3.69	28.42	13	39.42	3144 (+259/-236)	0.86 (+0.03/-0.04)	89.7	0.94	3043	—
124	23.96	12.97	4	53.26	2242 (+102/-94)	0.75 (+0.01/-0.02)	88.9	1.05	2062	—
125	24.79	12.85	2	44.25	2441 (+141/-134)	0.62 (+0.02/-0.02)	88.9	0.91	2262	—
126	25.54	12.80	5	36.31	2066 (+181/-157)	0.44 (+0.01/-0.02)	86.5	1.04	1891	—
127	24.55	11.98	5	45.49	2303 (+110/-94)	0.86 (+0.02/-0.02)	86.2	1.12	2123	—
128	25.46	11.76	4	43.53	2268 (+118/-110)	0.75 (+0.02/-0.02)	88.3	1.25	2088	—
129	26.17	11.74	4	47.47	2356 (+126/-118)	0.57 (+0.01/-0.02)	88.8	0.89	2175	—
130	27.12	11.17	6	43.58	2191 (+134/-126)	0.52 (+0.01/-0.02)	88.4	1.32	2013	—
131	26.58	10.62	5	42.18	2303 (+118/-102)	0.85 (+0.02/-0.02)	84.6	1.23	2123	—
132	28.25	10.08	10	34.23	2472 (+157/-157)	0.69 (+0.02/-0.02)	85.4	1.31	2294	—
133	27.47	10.05	2	25.62	2191 (+157/-149)	0.83 (+0.04/-0.03)	88.3	1.01	2013	—